

RealOSR: Latent Unfolding Boosting Diffusion-based Real-world Omnidirectional Image Super-Resolution

Xuhan Sheng[†], Runyi Li[†], Bin Chen, Weiqi Li, Xu Jiang, Jian Zhang[✉]
 School of Electronic and Computer Engineering, Peking University, China

{shengxuhan, lirunyi, chenbin, liweiqi}@stu.pku.edu.cn; jiangxu@scu.edu.cn
 zhangjian.sz@pku.edu.cn

Abstract

Omnidirectional image super-resolution (ODISR) aims to upscale low-resolution (LR) omnidirectional images (ODIs) to high-resolution (HR), addressing the growing demand for detailed visual content across a $180^\circ \times 360^\circ$ viewport. Existing methods are limited by simple degradation assumptions (e.g., bicubic downsampling), which fail to capture the complex, unknown real-world degradation processes. Recent diffusion-based approaches suffer from slow inference due to their hundreds of sampling steps and frequent pixel-latent space conversions. To tackle these challenges, in this paper, we propose RealOSR, a novel diffusion-based approach for real-world ODISR (Real-ODISR) with single-step diffusion denoising. To sufficiently exploit the input information, RealOSR introduces a lightweight domain alignment module, which facilitates the efficient injection of LR ODI into the single-step latent denoising. Additionally, to better utilize the rich semantic and multi-scale feature modeling ability of denoising UNet, we develop a latent unfolding module that simulates the gradient descent process directly in latent space. Experimental results demonstrate that RealOSR outperforms previous methods in both ODI recovery quality and efficiency. Compared to the recent state-of-the-art diffusion-based ODISR method, OmniSSR, RealOSR achieves significant improvements in visual quality and over $200\times$ inference acceleration. Our code and models will be released.

1. Introduction

Omnidirectional images (ODIs) can capture a viewport range of $180^\circ \times 360^\circ$, providing comprehensive visual information that enhances various applications. They have many projection methods like sphere projection (SP), equirectangular projection (ERP), and tangent projection (TP). In practice, ODIs require extremely high resolution (e.g. $4K \times 8K$ [1]) to display details in a narrow field of view (FoV). There-

fore, omnidirectional image super-resolution (ODISR) is proposed to reduce the industrial cost of high-precision camera sensors by super-resolving low-resolution (LR) ODIs into high-resolution (HR) counterparts.

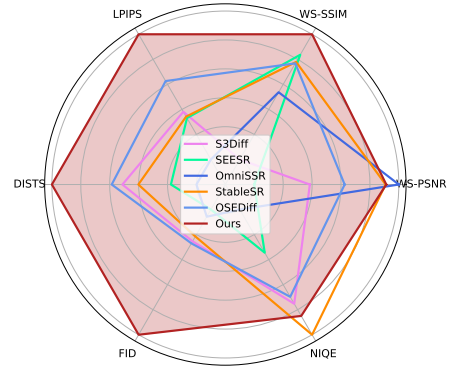
Diffusion models have emerged as next-generation visual generative models. From the pioneering work [44], these models are further developed by DDPM [17] and SDE [47]. Benefiting from diffusion-based image prior, the research of super-resolution (SR) has shifted the focus from simple degradations (e.g. bicubic downsampling) to real-world degradations, which has significantly developed real-world super-resolution (Real-SR) [53, 61, 66, 72]. Most of them use the high-order degradation pipeline of Real-ESRGAN [55] to simulate real-world degradations. Current methods for Real-SR primarily focus on planar images, with limited exploration of ODIs. Existing approaches for ODISR still face unsatisfactory performance. Most methods are end-to-end trained using pixel-level reconstruction loss (e.g. L_1 and L_2 losses) [11, 69], resulting in over-smoothed and distorted outputs. In addition, they use simple ERP-bicubic or fisheye-bicubic degradation, ignoring a range of unknown degradations that real-world omnidirectional camera sensors may encounter, struggling to achieve photo-realistic SR.

Recently, diffusion-based zero-shot image SR methods [9, 15, 20, 40, 58] leveraged pre-trained diffusion models for SR, incorporating LR images as conditions during the sampling process. Considering the characteristics of ODIs, OmniSSR [25] leverages the planar image generation priors in diffusion models to achieve ODISR without training. Although such zero-shot methods achieve superior performance, they need explicit degradation operator modeling. **Firstly**, the degradation pattern (denoted by operator \mathbf{A}) of the input ODI must be linear and fully known. Whereas in the real world, the degradation patterns are often nonlinear and unknown. **Secondly**, LR image conditioned guidance needs to be executed in pixel space, thus requiring repeated latent-pixel space conversions for updating denoising results using VAE. **Thirdly**, the ODI-oriented guidance on pixel space requires ERP \leftrightarrow TP transformation, which is

[†] Equal Contributor. [✉] Corresponding author.



(a) ERP and TP format of ODI-SR test-set image (id=20), and its restored results under real-world degradation. Zoom in for more detail.



(b) Metrics among current SR approaches and our method. We standardize the data as some metrics like FID lead to better results with a lower value.

Figure 1. Visualized and quantitative comparison of our method and other approaches, which demonstrates superior performance of both fidelity and visual realism of our method.

time-consuming.

Delving into the real-world ODISR (Real-ODISR) task, from experimental observations we draw our motivation as follows: (1) An approximate degradation guide still leads to a relatively significant performance improvement. This indicates that degradation information used for denoising guidance does not need to match the input LR image strictly and perfectly. Roughly accurate degradation information can still effectively guide the generation process. (2) In the SR task with bicubic degradation, \mathbf{A} and its inverse operator \mathbf{A}^\dagger used for denoising guidance [9, 25, 58] can be approximately regarded as a downsampler and upsampler, respectively. Such up/down-sampling in the latent space still preserves most of the original image information, similar to these operations in pixel space, suggesting that operations of \mathbf{A} , \mathbf{A}^\dagger could potentially be applied in the latent space, bypassing the need for pixel space.

Based on the aforementioned priors and insights, we propose **RealOSR**, a single-step denoising diffusion model designed to handle Real-ODISR task. Specifically, our method introduces the following key innovations: (1) **Integration of Real-World Degradation**: We incorporate real-world degradation into the ODISR task by developing degradation-aligned LR-HR image pairs for training and evaluation, ensuring that our model is trained and tested under conditions closely matching real-world scenarios. (2) **Latent Unfolding Guidance Module**: We present a deep unfolding-guided module that leverages degradation constraints as priors to guide the generation process at the latent space. This module enhances the model’s ability to adapt to specific degradation characteristics, improving the overall quality of the reconstructed images. (3) **Efficient Single-Step Sampling**: Our framework employs an efficient diffusion-based super-resolution method that utilizes single-step sampling, significantly reducing inference time. This efficiency not only

accelerates processing but also makes our algorithm suitable for real-world applications where timely results are crucial.

To summarize, our contributions are listed as follows:

- Toward the Real-ODISR task, we propose RealOSR, a diffusion model with deep unfolding injector guidance (DUIG) to achieve single-step denoising, and construct Real-ODISR datasets for effective model training and evaluation.
- The DUIG introduces a lightweight Domain Alignment Module (DAM) for explicit alignment and integration of LR images, along with a Latent Unfolding Module (LUM) for efficient degradation guidance in the latent space in single-step denoising.
- We conduct extensive performance validations on the constructed benchmark datasets, and our experimental results demonstrate the performance advantages and efficiency of our proposed framework, validating its effectiveness in real-world applications.

2. Related Work

2.1. Omnidirectional Image Super-Resolution

Image super-resolution methods based on generative adversarial networks (GANs) [5, 10, 36, 38, 55–57] often suffer from unstable training processes and pronounced visual artifacts. With the advent of diffusion models [7, 13, 47, 65], new inspiration has been brought to planar image super-resolution, resulting in a series of approaches aimed at handling simple degradation scenarios [8, 9, 20, 46, 58]. Recent studies [49, 53, 61, 66, 70, 70] have attempted to further improve real-world image super-resolution performance by introducing more powerful pre-trained models. PASD [66] extracts low-level and high-level information from the input and injects it into the diffusion process through a pixel-aware cross-attention module. SeeSR [61] incorporates tag-style text prompts and representation embeddings to guide the

diffusion process. SUPIR [70] leverages the powerful priors from LLaVA [31] and SDXL [39], pushing the visual quality boundaries of super-resolution tasks.

Although planar image super-resolution has advanced rapidly, ODISR remains underexplored. Recently, with the growing applications of ODISR in virtual reality, omnidirectional video streaming, and surveillance, researchers have increasingly focused on ODISR, proposing a series of methods [2–4, 6, 11, 25–27, 37, 50, 54, 69] to enhance the resolution of omnidirectional images. For instance, OmniSSR [25] utilizes Octadecaplex Tangent Information Interaction and Gradient Decomposition for zero-shot ODISR.

2.2. Efficient Diffusion Model Design

The sampling inefficiency of diffusion models has significantly hindered their development. [19, 33, 34, 45, 48] optimize numerical solvers to improve sampling speed. However, all solvers inherently introduce discretization bias, which affects the final sampling quality. [18, 30, 32, 41, 42, 63, 68] accelerate sampling from a distillation perspective. For example, Progressive Distillation [41] iteratively halves the number of sampling steps by distilling two Euler steps into a single Euler step. Consistency Models [48] generate high-quality samples by directly mapping noise to data. ADD [43] introduces adversarial loss during fractional distillation to improve high image fidelity. LADD [42] introduces Latent Adversarial Diffusion Distillation, further simplifying training and improving performance. In addition to distillation-based methods, several algorithms [22, 28] improve efficiency by optimizing the diffusion model structure. BK-SDM [22] removes certain residuals and attention modules in SD models to achieve lightweight design. SnapFusion [28] performs block pruning and channel pruning on the Unet and VAE decoder, reducing parameters and improving inference speed.

Recently, targeting the image restoration task, [60, 71, 72] use low-quality image information to shorten the Markov chain of the generation process. SinSR [59] proposes a one-step bidirectional distillation to learn the deterministic mapping between input noise and generated high-resolution images. Although promising results have been achieved in planar image super-resolution, the efficiency of ODISR lacks exploration. To the best of our knowledge, RealOSR is the first work for efficient real-world ODISR.

3. Method

3.1. Preliminaries

Diffusion-based Image Inverse Problem Solving In general, the image linear degradation problem can be modeled as $\mathbf{y} = \mathbf{A}\mathbf{x} + \mathbf{n}$, where \mathbf{y} represents the degraded image, \mathbf{A} is the linear degradation operator, \mathbf{x} is the original image, and \mathbf{n} is the random noise.

We typically refer to this type of problem as an *image*

inverse problem, and we can solve it using convex optimization techniques. Specifically, our optimization objective is formulated as:

$$\arg \min_{\mathbf{x}} \|\mathbf{y} - \mathbf{A}\mathbf{x}\|_2^2 + \lambda \mathcal{R}(\mathbf{x}). \quad (1)$$

It can be solved using gradient descent [73] iteratively:

$$\mathbf{x}^{k-1} = \mathbf{x}^k - \alpha \nabla_{\mathbf{x}^k} \|\mathbf{y} - \mathbf{A}\mathbf{x}^k\|_2^2, \quad (2)$$

where k denotes k -th optimizing step. The final solution, \mathbf{x}^0 , represents the reconstructed result.

In this optimization objective, $\|\mathbf{y} - \mathbf{A}\mathbf{x}\|_2^2$ ensures that the reconstruction result is consistent with the degraded input image, while the regularization term $\mathcal{R}(\mathbf{x})$ enforces image priors on \mathbf{x} , such as smoothness and sparsity.

In traditional methods for such an optimization problem, the regularization terms are typically represented as L1 norm, smooth functions, or total variation (TV) terms. While these terms improve the quality of generated images, their effectiveness is limited.

Diffusion models can provide robust visual priors, allowing the generated images to not only adhere to the consistency constraint $\mathbf{y} = \mathbf{A}\mathbf{x}$ but also align with natural image priors, as demonstrated in works such as DDNM [58] and DPS [9]. And the solving process is:

$$\begin{aligned} \mathbf{x}_{0|t} &= \frac{1}{\sqrt{\bar{\alpha}_t}} (\mathbf{x}_t + (1 - \bar{\alpha}_t) \epsilon_\theta) \\ \hat{\mathbf{x}}_{0|t} &= \mathbf{x}_{0|t} - \zeta \nabla \|\mathbf{y} - \mathbf{A}\mathbf{x}_{0|t}\|_2^2 \end{aligned} \quad (3)$$

For the gradient term $\nabla \|\mathbf{y} - \mathbf{A}\mathbf{x}_{0|t}\|_2^2$, we can simplify this via an approximate solution:

$$\hat{\mathbf{x}}_{0|t} = \mathbf{x}_{0|t} - \alpha (\mathbf{A}^\dagger \mathbf{A} \mathbf{x}_{0|t} - \mathbf{A}^\dagger \mathbf{y}) \quad (4)$$

Bridging Domain Gap with Projection Transformation

ERP images exhibit significant distortions and deformation in polar regions, which prevents them from directly applying planar image priors for ODISR. To bridge this domain gap, we can convert ERP images into TP images, which conform to the distribution of planar images. However, interpolation algorithms in projection transformation cause significant information loss, resulting in more blurred images.

We leverage the pre-upsampling strategy [25] by upsampling the source image before projection transformations. Specifically, at the input stage, the ERP image is first upsampled and then converted into TP images. At the output stage, the processed TP images are upsampled and then reprojected back into an ERP image to obtain the final output.

3.2. Motivation

In this section, we introduce our motivation, which supports gradient guidance in latent space, as follows:

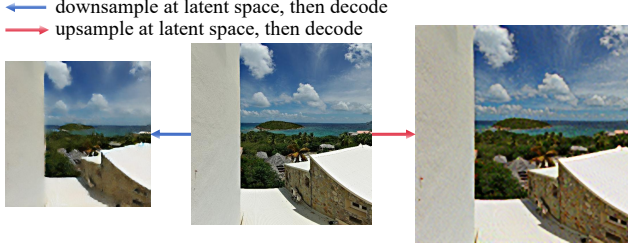


Figure 2. Bicubic up/down-sampling in latent space, decoded to pixel space for visualization. Despite minor damage, the original information is largely preserved, motivating us to apply deep unfolding directly in latent space.

ODI-SR Fisheye-bicubic $\times 4$	WS-PSNR \uparrow	WS-SSIM \uparrow	FID \downarrow
StableSR	23.19	0.6548	56.35
OmniSSR (ERP-bicubic)	25.21	0.7136	37.09

Table 1. Comparison of StableSR [38] and OmniSSR [25] performance on ODI-SR with fisheye-bicubic $\times 4$ downsampling. Despite using ERP-bicubic as guidance, OmniSSR surpasses its baseline model StableSR in overall performance. Suggesting the degradation for guidance does not need to precisely match the degradation of the input image. Best results are shown in **bold**.

Condition Guidance in Latent Diffusion. Previous latent-based diffusion models, such as PSLD [40], perform denoising sampling in the latent space and use VAE to convert the results to pixel space for gradient updates, requiring VAE back-propagation and incurring additional memory and time costs. While OmniSSR introduces a condition-guidance technique that avoids back-propagating through VAE, it still requires conversion of latent and pixel spaces at each step, thus not fully resolving VAE-related inefficiencies.

Unknown Degradation. A preliminary experiment was conducted (see Tab. 1) with fisheye-bicubic downsampling [69] to generate LR ODIs, while the degradation guidance in OmniSSR is modeled as ERP-bicubic downsampling. OmniSSR still outperforms its base model, StableSR, across WS-PSNR, WS-SSIM, and FID. This suggests that the degradation operator \mathbf{A} in OmniSSR need not precisely match the input image degradation; an approximate degradation operator can still effectively guide the diffusion model to achieve better results. Inspired by DKP’s proposal [67] for dynamic degradation estimation, we propose using a learnable operator to dynamically adapt to image-specific degradation conditions, supporting efficient deep unfolding in latent space with improved speed and reduced memory.

Degradation Correspondence in Latent Space. Latent and pixel spaces, though distinct, exhibit strong correspondence. In SR tasks with bicubic downsampling, the degradation operator \mathbf{A} and its pseudo-inverse \mathbf{A}^\dagger correspond to specific downsampling and upsampling operations. We apply them directly in the latent space with results visualized in pixel space (Fig. 2). While the up/down-sampled images show certain damage, the semantic and structural informa-

tion remains largely preserved. This motivates leveraging deep unfolding in latent space, where feature representations are semantically richer, making it better suited for addressing complex, real-world non-linear degradation.

3.3. Overview

Our method (shown in Algo. 1) can be divided as follows:

- ① The ERP image \mathbf{E}_{LR} is converted into TP images $\{\mathbf{x}_{LR}^1, \mathbf{x}_{LR}^2, \dots, \mathbf{x}_{LR}^M\}$ using the ERP \rightarrow TP transformation (denoted as $\mathcal{F}(\cdot)$). A pre-trained degradation predictor [36] then outputs the levels of *noise* and *blur* in a 2-dimensional vector, $\mathbf{d} = [d_n, d_b] \in [0, 1]^2$, based on the TP images.
- ② These TP images are fed into the Stable Diffusion (SD) encoder to obtain latent representations. After a single denoising step by the SD UNet ϵ_θ , the output is decoded back into TP images, which are subsequently reprojected to form the final high-resolution ERP image via the TP \rightarrow ERP transformation (denoted as $\mathcal{F}^{-1}(\cdot)$). During the UNet forward, $\mathbf{d} = [d_n, d_b]$ generates degradation-aware LoRA [72] for UNet blocks, SD VAE Encoder, and modulates parameters for Deep Unfolding Injection Guidance.
- ③ During training, the SD VAE decoder \mathcal{D} and degradation predictor remain frozen. The SD VAE encoder \mathcal{E} and UNet ϵ_θ are fine-tuned with degradation-aware LoRA, while the parameters in the DUIG undergo full training.

Algorithm 1: RealOSR Pipeline

Input: Input LR ERP image \mathbf{E}_{LR} , ERP \rightarrow TP & TP \rightarrow ERP transformations: \mathcal{F} & \mathcal{F}^{-1} , degradation predictor DP, SD denoising UNet ϵ_θ , SD VAE Encoder & Decoder \mathcal{E} & \mathcal{D}

Output: SR result $\tilde{\mathbf{E}}$

- 1 $\{\mathbf{x}_{LR}^{(1)}, \mathbf{x}_{LR}^{(2)}, \dots, \mathbf{x}_{LR}^{(M)}\} = \mathcal{F}(\mathbf{E}_{LR})$
- 2 **for** $m = 1$ **to** M **do**
- 3 $d_n, d_b = \text{DP}(\mathbf{x}_{LR}^{(m)})$
- 4 LoRA_weights = Embedding(d_n, d_b)
- 5 $\mathcal{E}.\text{load_weight}(\text{LoRA_weights})$
- 6 $\epsilon_\theta.\text{load_weight}(\text{LoRA_weights})$
- 7 $\mathbf{z}^{(m)} = \mathcal{E}(\mathbf{x}_{LR}^{(m)})$
- 8 Get denoised latent code $\tilde{\mathbf{z}}^{(m)}$ using Algo. 2
- 9 $\tilde{\mathbf{x}}^{(m)} = \mathcal{D}(\tilde{\mathbf{z}}^{(m)})$
- 10 **end**
- 11 $\tilde{\mathbf{E}} = \mathcal{F}^{-1}(\{\tilde{\mathbf{x}}^{(1)}, \tilde{\mathbf{x}}^{(2)}, \dots, \tilde{\mathbf{x}}^{(M)}\})$
- 12 **return** $\tilde{\mathbf{E}}$

3.4. Deep Unfolding Injection Guidance

The insights in Sec. 3.2 motivate us to achieve real-world degradation-based deep unfolding in the latent space. To further achieve single-step denoising, we refer to implementing latent-based deep unfolding between UNet blocks. **For simplicity, here the “latent space” refers to the whole feature space expanded by each UNet block in contrast to pixel space.**

Domain Alignment Module (DAM). Since the pixel space of the conditional LR image and the latent space expanded by the UNet blocks have a large domain gap, we

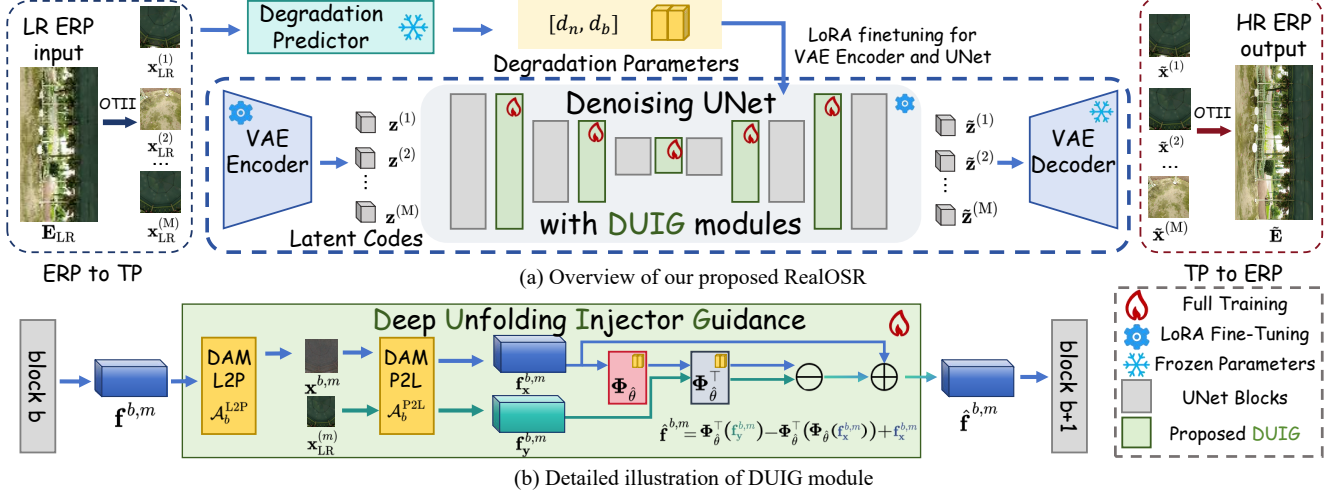


Figure 3. Overall architecture and detailed Deep Unfolding Injector Guidance of our proposed RealOSR. Input LR ERP is first transformed into TP images, and then sent sequentially through the SD encoder into denoising UNet with (1) degradation-aware LoRA, and (2) DUIG for LR information guidance. All generated TP images are transformed back to ERP format to obtain the final SR result.

propose the domain alignment module (DAM) composed of latent-to-pixel (L2P) and pixel-to-latent (P2L) to achieve the conversion between the latent space and the pixel space, thus supporting efficient information injection. Meanwhile, the latent spaces expanded by different UNet blocks are different, a series of DAMs are required for each UNet block. Therefore, the DAM consists of channel shuffle and group convolution to ensure parameter efficiency.

Specifically, for the m -th TP image, the feature map $\mathbf{f}^{b,m}$ output by the b -th UNet block, the conversions are achieved as follows:

$$\begin{aligned} \mathbf{x}^{b,m} &= \mathcal{A}_b^{\text{L2P}}(\mathbf{f}^{b,m}), \\ \mathbf{f}_x^{b,m} &= \mathcal{A}_b^{\text{P2L}}(\mathbf{x}^{b,m}), \\ \mathbf{f}_y^{b,m} &= \mathcal{A}_b^{\text{P2L}}(\mathbf{x}_{\text{LR}}^{(m)}), \end{aligned} \quad (5)$$

where $\mathcal{A}_b^{\text{L2P}}(\cdot)$ converts feature maps from the b -th UNet block into pixel space, allowing for pixel-level control when necessary. Conversely, $\mathcal{A}_b^{\text{P2L}}(\cdot)$ enables efficient mapping back to the latent space of the b -th UNet block, supporting latent-level control, such as the latent unfolding module. DAM is designed to be lightweight by utilizing 1×1 convolutions and Channel Shuffle [75] for efficient feature transformation while employing pixel shuffle/unshuffle operations for fast up/down-sampling.

Latent Unfolding Module (LUM). Gradient descent-based deep unfolding is trivial when \mathbf{A} is linear and known. In real-world ODISR, however, the degradation operator Φ is non-linear and unknown, making gradient calculation in Eq. 4 intractable. To address this, we propose the Latent Unfolding Module (LUM), which parameterizes $\Phi_{\hat{\theta}}(\cdot)$ and $\Phi_{\hat{\theta}}^{\top}(\cdot)$ to simulate the role of \mathbf{A} and \mathbf{A}^{\dagger} during the gradient descent step under non-linear degradation. Leveraging the rich semantic and multi-scale information within the latent

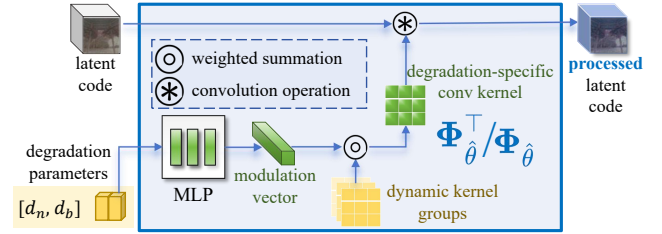


Figure 4. Details of $\Phi_{\hat{\theta}}(\cdot)$ and $\Phi_{\hat{\theta}}^{\top}(\cdot)$, both designed as 3×3 degradation-aware dynamic convolutions. Despite having identical network structures, they do not share learned parameters' weights.

spaces from UNet blocks, the simulated gradient descent is performed in the latent spaces:

$$\hat{\mathbf{f}}^{b,m} = \mathbf{f}_x^{b,m} + \Phi_{\hat{\theta}}^{\top}(\mathbf{f}_y^{b,m}) - \Phi_{\hat{\theta}}^{\top}(\Phi_{\hat{\theta}}(\mathbf{f}_x^{b,m})). \quad (6)$$

In the context of the image linear inverse problem, \mathbf{A} and \mathbf{A}^{\dagger} represent degradation characteristics. Specifically, in the SR task, they are typically modeled using hand-crafted parametrized convolution kernels [58]. Inspired by this, the proposed $\Phi_{\hat{\theta}}(\cdot)$ and $\Phi_{\hat{\theta}}^{\top}(\cdot)$ are designed to adapt to different degradation types by using 3×3 dynamic convolution [24], where $\hat{\theta}$ includes parameters of MLP-based dynamic weight generator and the convolution kernel groups which are dynamically assembled based on degradation parameters $\mathbf{d} = [d_n, d_b]$, as illustrated in Fig. 4.

Via this way, the unconditional generation process of SD can incorporate degradation information as guidance, resulting in SR results that balance fidelity and realism. The detailed algorithm for the DUIG is shown as Algo. 2.

Datasets	Methods	WS-PSNR \uparrow	WS-SSIM \uparrow	LPIPS \downarrow	DISTS \downarrow	FID \downarrow	NIQE \downarrow	MUSIQ \uparrow	MANIQA \uparrow	CLIPQA \uparrow
ODI-SR	S3Diff	20.91	0.4606	0.4197	0.1649	85.01	3.6173	66.53	0.4759	0.5639
	SeeSR	19.89	0.5629	0.4411	0.2234	126.21	4.9682	64.94	0.4884	0.7141
	OmniSSR	22.53	0.5263	0.6638	0.2747	113.79	7.2586	26.05	0.2275	0.2346
	StableSR	22.29	0.5559	0.4359	0.1804	89.48	3.1052	58.28	0.3072	0.4393
	OSDiff	21.54	0.5545	0.3394	0.1559	83.27	3.7561	68.56	0.4923	0.6301
	RealOSR (Ours)	22.30	0.5829	0.2628	0.1194	43.39	3.3973	68.08	0.4117	0.6436
SUN 360	S3Diff	21.45	0.5015	0.4343	0.1520	94.67	3.3212	68.74	0.5088	0.5455
	SeeSR	20.01	0.5933	0.4403	0.2164	125.78	5.3113	70.54	0.5462	0.6795
	OmniSSR	22.39	0.5220	0.7029	0.2889	140.32	7.3032	26.92	0.2165	0.2186
	StableSR	22.55	0.5804	0.4663	0.1780	105.85	3.3234	57.60	0.3027	0.3977
	OSDiff	21.99	0.5921	0.3692	0.1502	85.54	3.6205	70.44	0.5111	0.5900
	RealOSR (Ours)	22.70	0.6171	0.2888	0.1047	41.69	3.4615	69.64	0.4198	0.6080

Table 2. Quantitative comparison with state-of-the-art diffusion-based methods of ODISR and Real-SR. The best and second-best results of each metric are highlighted in **red** and **blue**, respectively.

Datasets	Methods	WS-PSNR \uparrow	WS-SSIM \uparrow	LPIPS \downarrow	DISTS \downarrow	FID \downarrow	NIQE \downarrow	MUSIQ \uparrow	MANIQA \uparrow	CLIPQA \uparrow
ODI-SR	SwinIR	24.23	0.6546	0.4887	0.2695	88.92	7.2417	42.13	0.2854	0.3739
	OSRT	24.36	0.6589	0.4855	0.2679	84.60	7.1720	44.50	0.3172	0.3965
	RealOSR (Ours)	22.30	0.5829	0.2628	0.1194	43.39	3.3973	68.08	0.4117	0.6436
SUN 360	SwinIR	24.35	0.6808	0.4977	0.2578	88.17	7.2570	44.72	0.2747	0.3354
	OSRT	24.55	0.6862	0.4841	0.2538	82.00	7.0799	49.21	0.3225	0.3640
	RealOSR (Ours)	22.70	0.6171	0.2888	0.1047	41.69	3.4615	69.64	0.4198	0.6080

Table 3. Quantitative comparison with end-to-end SR methods on ODI-SR and SUN 360 datasets. The best results are shown in **red**.

Algorithm 2: UNet Denoising with DUIG

Input: $\mathbf{z}_{LR}^{(m)}, \epsilon_\theta = \{\text{Block}_1, \text{Block}_2, \dots, \text{Block}_B\}, \mathbf{x}_{LR}^{(m)}, \Phi_\theta, \Phi_\theta^\top$
Output: Denoised latent code $\tilde{\mathbf{z}}^{(m)}$

- 1 $\hat{\mathbf{f}}_x^{0,m} = \mathbf{z}^{(m)}$
- 2 **for** $b = 1$ **to** B **do**
- 3 $\mathbf{f}_x^{b,m} = \text{Block}_b(\hat{\mathbf{f}}^{b-1,m})$
- 4 /* Domain Alignment Module */
- 5 $\mathbf{x}^{b,m} = \mathcal{A}_b^{\text{L2P}}(\mathbf{f}_x^{b,m})$,
- 6 $\mathbf{f}_x^{b,m} = \mathcal{A}_b^{\text{P2L}}(\mathbf{x}^{b,m})$,
- 7 $\mathbf{f}_y^{b,m} = \mathcal{A}_b^{\text{P2L}}(\mathbf{x}_{LR}^{(m)})$.
- 8 /* Latent Unfolding Module */
- 9 $\hat{\mathbf{f}}^{b,m} = \mathbf{f}_x^{b,m} + \Phi_\theta^\top(\mathbf{f}_y^{b,m}) - \Phi_\theta^\top(\Phi_\theta(\mathbf{f}_x^{b,m}))$
- 10 **end**
- 11 $\tilde{\mathbf{z}}^{(m)} = \hat{\mathbf{f}}_x^{B,m}$
- 12 **return** $\tilde{\mathbf{z}}^{(m)}$

3.5. Training Details

In our proposed RealOSR, the VAE decoder and the degradation predictor remain frozen, requiring no training. The SD UNet and VAE encoder are trained with LoRA conditioned on degradation parameters, enabling dynamic, data-dependent adjustments to model parameters in response to specific degradation. All weights in the DUIG undergo training.

Following S3Diff [72], we employ a comprehensive loss function and use adversarial learning to further enhance the realness of the SR results. The total loss is defined as:

$$\mathcal{L}_{total} = \lambda_{\text{rec}}\mathcal{L}_{\text{rec}} + \lambda_{\text{LPIPS}}\mathcal{L}_{\text{LPIPS}} + \lambda_{\text{GAN}}\mathcal{L}_{\text{GAN}}. \quad (7)$$

Here, a differentiable variant of L1 Loss, named Charbonnier Loss [23], is employed as the pixel-level reconstruction loss \mathcal{L}_{rec} , complemented by LPIPS Loss $\mathcal{L}_{\text{LPIPS}}$ and GAN Loss \mathcal{L}_{GAN} to reduce the data distribution distance between SR results and HR ODIs.

Compared to directly applying ERP-bicubic downsampling [12], OSRT [69] introduces fisheye-bicubic downsampling to more accurately simulate real-world degradation in originally captured fisheye-formatted images, accounting for degradation that typically results from limited sensor precision and density before conversion into other storage formats. However, degradation occurring during the real-world capture of raw images is usually unknown and more complex than simple bicubic downsampling. Therefore, we apply the degradation pipeline proposed in Real-ESRGAN [55] to the fisheye images and subsequently convert them into LR ERP images to simulate real-world degradation.

4. Experiments

4.1. Implementation Details

Datasets and Pretrained Models. We use ODI-SR dataset from LAU-Net [11] and SUN 360 Panorama dataset [62], where HR ERP images are of resolution 1024×2048 . The $\times 4$ downsampling degradation pipeline of Real-ESRGAN [55] is performed on HR fisheye images and stored as LR ERP images. For the Stable Diffusion model, we choose the

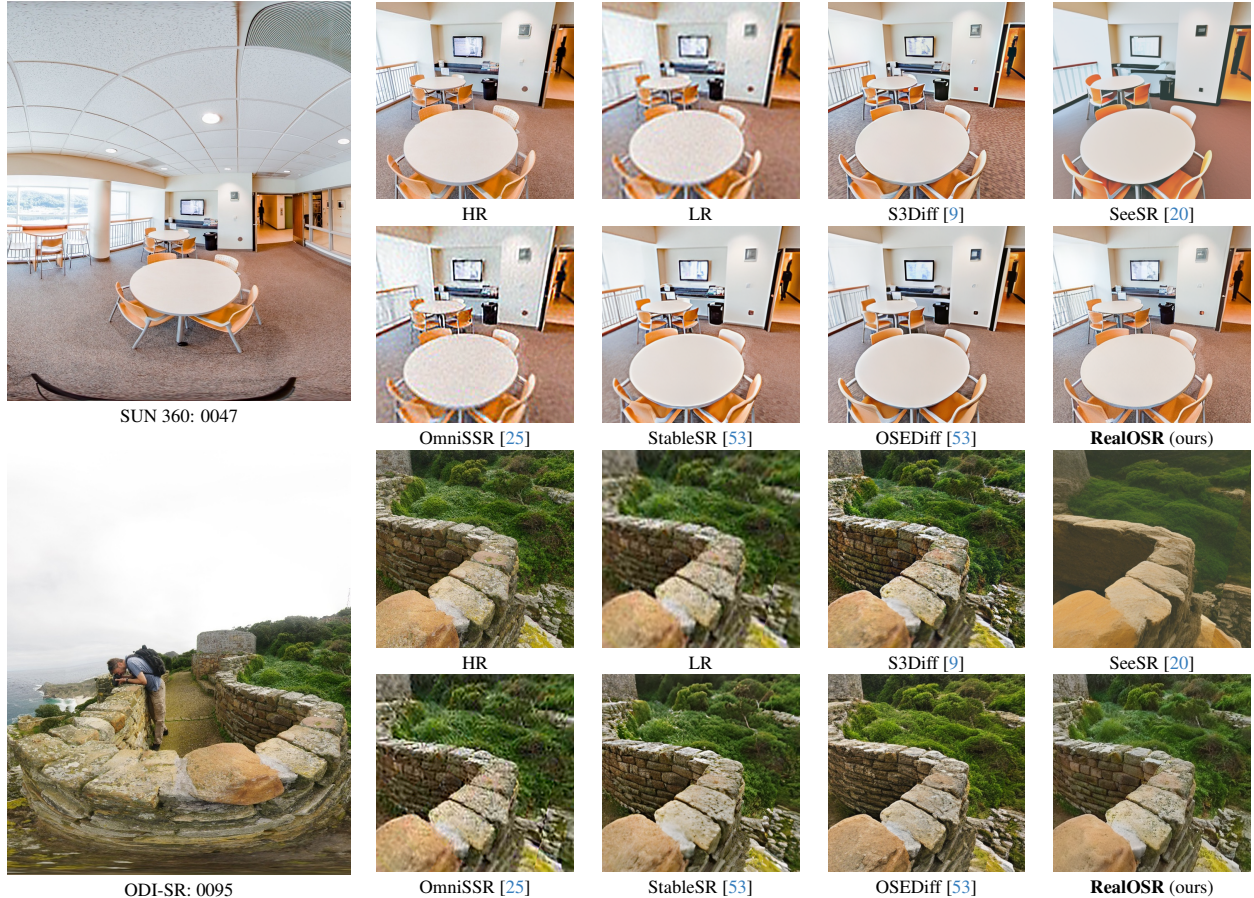


Figure 5. Visualized comparison of SR results on SUN 360 test set and ODI-SR test set. 0047 and 0095 are the ID numbers in the test set filenames. Our RealOSR can achieve photo-realistic SR results compared to other diffusion-based methods.

version SD-Turbo.

Training settings The hyperparameters λ_{rec} , λ_{LPIPS} , λ_{GAN} in are set as 2, 5, and 0.5, respectively. Adam is used for optimization with a learning rate of $1e-5$, and a total batch size of 4. All experiments are conducted on NVIDIA 4090 GPU.

Evaluation Metrics. To comprehensively assess the performance of various methods, we employ both reference and non-reference metrics. WS-PSNR [51] and WS-SSIM [76] are reference-based fidelity metrics computed on RGB channels. LPIPS [74] and DISTS [14] serve as reference-based perceptual quality metrics, while FID [16] measures the distribution distance between ground truth and SR images. Additionally, NIQE [35], MANIQA [64], MUSIQ [21], and CLIPQA [52] are used as non-reference metrics.

4.2. Evaluation of RealOSR

In this section, we evaluate the proposed RealOSR, categorizing the methods for comparison into two groups: (1)

Link is here: <https://huggingface.co/stabilityai/sd-turbo>

diffusion-based SR methods, including S3Diff [72], SeeSR [61], OmniSSR [25], StableSR [53], and OSEDiff [60]; (2) end-to-end trained SR methods, including OSRT [69] and SwinIR [29].

Comparison with diffusion-based SR methods are shown in Tab. 2 and the visual results are presented in Fig. 5. Our method demonstrates a marked improvement in both fidelity and realism compared to existing diffusion-based SR methods. While SeeSR achieves higher scores on non-reference metrics (NIQE, MANIQA, MUSIQ, CLIPQA), the visualizations in Fig. 5 reveal that SeeSR’s SR outputs exhibit blurred, painterly texture that is clearly inferior to the outputs of other methods. This discrepancy likely arises because these non-reference metrics, designed for planar images, do not accurately assess model performance in the ODISR context.

Comparison with end-to-end trained SR methods are shown in Tab. 3 and the visual results are presented in Fig. 6. Our method has superior photo-realistic fidelity and visual realism compared to end-to-end training methods, avoiding over-smooth and distorted visual content.

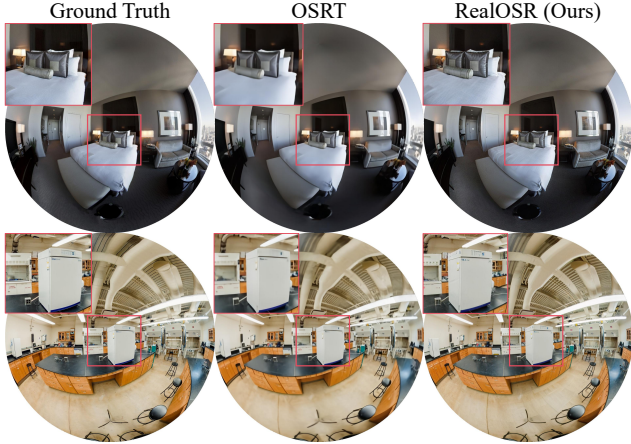


Figure 6. Comparison between OSRT and our RealOSR displayed in fisheye projection. Zoom in for more details.

Method	LPIPS↓	DISTS↓	FID↓
① S3Diff (TP)	0.2763	0.1203	49.78
② RealOSR (Latent-Add)	0.2686	0.1246	45.81
③ RealOSR (Pixel-Unfold)	0.2669	0.1252	46.35
④ RealOSR	0.2628	0.1194	43.39

Table 4. Ablation results of DUIG, best results shown in red.

4.3. Ablation Study

This ablation study investigates the contributions of the Domain Alignment Module (DAM) and Latent Unfolding Module (LUM) within DUIG. The following model variants are considered: ① S3Diff (TP): S3Diff fine-tuned with TP images as input; ② RealOSR (Latent-Add): LUM is replaced by directly adding $f_y^{b,m}$ and $f_x^{b,m}$ within DUIG; ③ RealOSR (Pixel-Unfold): LUM is applied in the pixel space within DUIG; ④ RealOSR: The full proposed model.

The quantitative results in Tab. 4 show that: (1) Comparing ① and ② demonstrates that DAM facilitates efficient alignment and integration of LR image information, leading to certain performance improvements. (2) Comparing ② and ④ highlights that LUM provides more effective degradation guidance compared to simply adding information from the LR image. (3) Comparing ③ and ④ reveals that deep unfolding in the latent space enables more accurate modeling of real-world degradation guidance.

4.4. Discussion

We select the weights of nine channels from the 3×3 degradation-aware convolution kernels in Latent Unfolding Module and visualize their variations with respect to different input degradation parameters. As shown in Fig. 7, the degradation-aware convolution kernels in Φ_θ and Φ_θ^\top exhibit distinct patterns adaptively according to the varying degradation parameters.

The aforementioned experiments reveal the following dis-

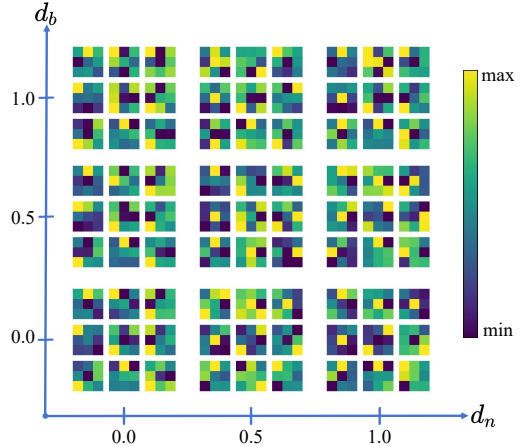


Figure 7. Degradation-specific kernel weights in the DUIG after the SD UNet bottleneck, dynamically adjust with changing degradation parameters. Nine channels in 3×3 convolution kernels illustrate representative results for the specific noise and blur $[d_n, d_b]$.

cussions: (1) The comparison in Sec. 4.2 shows that present non-reference metrics designed for planar images are insufficient for accurately evaluating ODISR performance. Future work can focus on developing evaluation metrics tailored for ODI’s visual quality assessment. (2) The proposed RealOSR model relies on the computationally intensive Stable Diffusion model, which currently limits its deployment on edge devices. Future work could explore lightweight alternatives to enable feasible deployment on resource-constrained devices, expanding RealOSR’s practical applicability across a wider range of environments and platforms. (3) The degradation-aware convolution in the Latent Unfolding Module effectively leverages the denoising UNet’s semantic and multi-scale feature modeling capabilities. However, a suitable visualization method is needed to fully demonstrate its effectiveness.

5. Conclusion

In this paper, we proposed a novel method, RealOSR, for real-world omnidirectional image super-resolution (Real-ODISR) by providing a more effective and efficient solution to real degradations compared to previous approaches. RealOSR integrated real-world degradation into the latent unfolding guidance module and employs efficient single-step diffusion sampling, empirically validated to enhance the fidelity and realism of the super-resolution results. These designs not only improved performance on current benchmarks but also established a new baseline for further research in Real-ODISR. Future work could focus on enabling real-time applications in fields like virtual reality and live broadcasting by further improving the model’s efficiency.

References

- [1] Hao Ai, Zidong Cao, Jinjing Zhu, Haotian Bai, Yucheng Chen, and Ling Wang. Deep learning for omnidirectional vision: A survey and new perspectives. *arXiv preprint arXiv:2205.10468*, 2022. 1
- [2] Hongyu An and Xinfeng Zhang. Perception-oriented omnidirectional image super-resolution based on transformer network. In *Proceedings of the IEEE International Conference on Image Processing (ICIP)*, 2023. 3
- [3] Zafer Arican and Pascal Frossard. Joint registration and super-resolution with omnidirectional images. *IEEE Transactions on Image Processing (TIP)*, 2011.
- [4] Mingdeng Cao, Chong Mou, Fanghua Yu, Xintao Wang, Yinqiang Zheng, Jian Zhang, Chao Dong, Gen Li, Ying Shan, Radu Timofte, et al. Ntire 2023 challenge on 360deg omnidirectional image and video super-resolution: Datasets, methods and results. In *Proceedings of the IEEE/CVF Conference on Computer Vision and Pattern Recognition Workshops (CVPRW)*, 2023. 3
- [5] Kelvin CK Chan, Xiangyu Xu, Xintao Wang, Jinwei Gu, and Chen Change Loy. Glean: Generative latent bank for image super-resolution and beyond. *IEEE Transactions on Pattern Analysis and Machine Intelligence (TPAMI)*, 2022. 2
- [6] Ming Cheng, Haoyu Ma, Qiufang Ma, Xiaopeng Sun, Weiqi Li, Zhenyu Zhang, Xuhan Sheng, Shijie Zhao, Junlin Li, and Li Zhang. Hybrid transformer and cnn attention network for stereo image super-resolution. In *Proceedings of the IEEE/CVF Conference on Computer Vision and Pattern Recognition (CVPR)*, 2023. 3
- [7] Jooyoung Choi, Sungwon Kim, Yonghyun Jeong, Youngjune Gwon, and Sungroh Yoon. Ilvr: Conditioning method for denoising diffusion probabilistic models. In *Proceedings of the IEEE/CVF International Conference on Computer Vision (ICCV)*, 2021. 2
- [8] Hyungjin Chung, Byeongsu Sim, and Jong Chul Ye. Improving diffusion models for inverse problems using manifold constraints. In *Proceedings of the Advances in Neural Information Processing Systems (NeurIPS)*, 2022. 2
- [9] Hyungjin Chung, Jeongsol Kim, Michael Thompson Mccann, Marc Louis Klasky, and Jong Chul Ye. Diffusion posterior sampling for general noisy inverse problems. In *Proceedings of the International Conference on Learning Representations (ICLR)*, 2023. 1, 2, 3, 7
- [10] Giannis Daras, Joseph Dean, Ajil Jalal, and Alex Dimakis. Intermediate layer optimization for inverse problems using deep generative models. In *Proceedings of the International Conference on Machine Learning (ICML)*, 2021. 2
- [11] Xin Deng, Hao Wang, Mai Xu, Yichen Guo, Yuhang Song, and Li Yang. Lau-net: Latitude adaptive upscaling network for omnidirectional image super-resolution. In *Proceedings of the IEEE/CVF Conference on Computer Vision and Pattern Recognition (CVPR)*, 2021. 1, 3, 6
- [12] Xin Deng, Hao Wang, Mai Xu, Li Li, and Zulin Wang. Omnidirectional image super-resolution via latitude adaptive network. *IEEE Transactions on Multimedia (TMM)*, 2022. 6
- [13] Prafulla Dhariwal and Alexander Nichol. Diffusion models beat gans on image synthesis. In *Proceedings of the Advances in Neural Information Processing Systems (NeurIPS)*, 2021. 2
- [14] Keyan Ding, Kede Ma, Shiqi Wang, and Eero P Simoncelli. Image quality assessment: Unifying structure and texture similarity. *IEEE Transactions on Pattern Analysis and Machine Intelligence (TPAMI)*, 2020. 7
- [15] Ben Fei, Zhaoyang Lyu, Liang Pan, Junzhe Zhang, Weidong Yang, Tianyue Luo, Bo Zhang, and Bo Dai. Generative diffusion prior for unified image restoration and enhancement. In *Proceedings of the IEEE/CVF Conference on Computer Vision and Pattern Recognition (CVPR)*, 2023. 1
- [16] Martin Heusel, Hubert Ramsauer, Thomas Unterthiner, Bernhard Nessler, and Sepp Hochreiter. Gans trained by a two time-scale update rule converge to a local nash equilibrium. In *Proceedings of the Advances in Neural Information Processing Systems (NeurIPS)*, 2017. 7
- [17] Jonathan Ho, Ajay Jain, and Pieter Abbeel. Denoising diffusion probabilistic models. In *Proceedings of the Advances in Neural Information Processing Systems (NeurIPS)*, 2020. 1
- [18] Minguk Kang, Richard Zhang, Connelly Barnes, Sylvain Paris, Suha Kwak, Jaesik Park, Eli Shechtman, Jun-Yan Zhu, and Taesung Park. Distilling diffusion models into conditional gans. In *Proceedings of the European Conference on Computer Vision (ECCV)*, 2024. 3
- [19] Tero Karras, Miika Aittala, Timo Aila, and Samuli Laine. Elucidating the design space of diffusion-based generative models. In *Proceedings of the Advances in Neural Information Processing Systems (NeurIPS)*, 2022. 3
- [20] Bahjat Kawar, Michael Elad, Stefano Ermon, and Jiaming Song. Denoising diffusion restoration models. In *Proceedings of the Advances in Neural Information Processing Systems (NeurIPS)*, 2022. 1, 2, 7
- [21] Junjie Ke, Qifei Wang, Yilin Wang, Peyman Milanfar, and Feng Yang. Musiq: Multi-scale image quality transformer. In *Proceedings of the IEEE/CVF International Conference on Computer Vision (ICCV)*, 2021. 7
- [22] Bo-Kyeong Kim, Hyoung-Kyu Song, Thibault Castells, and Shinkook Choi. Bk-sdm: A lightweight, fast, and cheap version of stable diffusion. In *Proceedings of the European Conference on Computer Vision (ECCV)*, 2024. 3
- [23] Wei-Sheng Lai, Jia-Bin Huang, Narendra Ahuja, and Ming-Hsuan Yang. Deep laplacian pyramid networks for fast and accurate super-resolution. In *Proceedings of the IEEE Conference on Computer Vision and Pattern Recognition (CVPR)*, 2017. 6
- [24] Chao Li, Aojun Zhou, and Anbang Yao. Omni-dimensional dynamic convolution. In *Proceedings of the International Conference on Learning Representations (ICLR)*, 2022. 5
- [25] Runyi Li, Xuhan Sheng, Weiqi Li, and Jian Zhang. Omnissr: Zero-shot omnidirectional image super-resolution using stable diffusion model. In *Proceedings of the European Conference on Computer Vision (ECCV)*, 2024. 1, 2, 3, 4, 7
- [26] Weiqi Li, Bin Chen, and Jian Zhang. D3c2-net: Dual-domain deep convolutional coding network for compressive sensing. *IEEE Transactions on Circuits and Systems for Video Technology (TCSVT)*, 2024.
- [27] Weiqi Li, Shijie Zhao, Bin Chen, Xinhua Cheng, Junlin Li, Li Zhang, and Jian Zhang. Resvr: Joint rescaling and viewport

- rendering of omnidirectional images. In *Proceedings of the 32nd ACM International Conference on Multimedia (ACM MM)*, 2024. 3
- [28] Yanyu Li, Huan Wang, Qing Jin, Ju Hu, Pavlo Chemerys, Yun Fu, Yanzhi Wang, Sergey Tulyakov, and Jian Ren. Snapfusion: Text-to-image diffusion model on mobile devices within two seconds. In *Proceedings of the Advances in Neural Information Processing Systems (NeurIPS)*, 2024. 3
- [29] Jingyun Liang, Jiezhong Cao, Guolei Sun, Kai Zhang, Luc Van Gool, and Radu Timofte. Swinir: Image restoration using swin transformer. In *Proceedings of the IEEE/CVF International Conference on Computer Vision Workshops (ICCVW)*, 2021. 7
- [30] Shanchuan Lin, Anran Wang, and Xiao Yang. Sdxl-lightning: Progressive adversarial diffusion distillation. *arXiv preprint arXiv:2402.13929*, 2024. 3
- [31] Haotian Liu, Chunyuan Li, Qingyang Wu, and Yong Jae Lee. Visual instruction tuning. In *Proceedings of the Advances in Neural Information Processing Systems (NeurIPS)*, 2024. 3
- [32] Xingchao Liu, Chengyue Gong, et al. Flow straight and fast: Learning to generate and transfer data with rectified flow. In *Proceedings of the International Conference on Learning Representations (ICLR)*, 2023. 3
- [33] Cheng Lu, Yuhao Zhou, Fan Bao, Jianfei Chen, Chongxuan Li, and Jun Zhu. Dpm-solver: A fast ode solver for diffusion probabilistic model sampling in around 10 steps. In *Proceedings of the Advances in Neural Information Processing Systems (NeurIPS)*, 2022. 3
- [34] Cheng Lu, Yuhao Zhou, Fan Bao, Jianfei Chen, Chongxuan Li, and Jun Zhu. Dpm-solver++: Fast solver for guided sampling of diffusion probabilistic models. *arXiv preprint arXiv:2211.01095*, 2022. 3
- [35] Anish Mittal, Rajiv Soundararajan, and Alan C. Bovik. Making a “completely blind” image quality analyzer. *IEEE Signal Processing Letters (SPL)*, 2013. 7
- [36] Chong Mou, Yanze Wu, Xintao Wang, Chao Dong, Jian Zhang, and Ying Shan. Metric learning based interactive modulation for real-world super-resolution. In *Proceedings of the European Conference on Computer Vision (ECCV)*, 2022. 2, 4
- [37] Akito Nishiyama, Satoshi Ikehata, and Kiyoharu Aizawa. 360° single image super resolution via distortion-aware network and distorted perspective images. In *Proceedings of the IEEE International Conference on Image Processing (ICIP)*, 2021. 3
- [38] Xingang Pan, Xiaohang Zhan, Bo Dai, Dahua Lin, Chen Change Loy, and Ping Luo. Exploiting deep generative prior for versatile image restoration and manipulation. *IEEE Transactions on Pattern Analysis and Machine Intelligence (TPAMI)*, 2021. 2, 4
- [39] Dustin Podell, Zion English, Kyle Lacey, Andreas Blattmann, Tim Dockhorn, Jonas Müller, Joe Penna, and Robin Rombach. Sdxl: Improving latent diffusion models for high-resolution image synthesis. In *Proceedings of the International Conference on Learning Representations (ICLR)*, 2024. 3
- [40] Litu Rout, Negin Raoof, Giannis Daras, Constantine Caramanis, Alex Dimakis, and Sanjay Shakkottai. Solving linear inverse problems provably via posterior sampling with latent diffusion models. In *Proceedings of the Advances in Neural Information Processing Systems (NeurIPS)*, 2023. 1, 4
- [41] Tim Salimans and Jonathan Ho. Progressive distillation for fast sampling of diffusion models. In *Proceedings of the International Conference on Learning Representations (ICLR)*, 2022. 3
- [42] Axel Sauer, Frederic Boesel, Tim Dockhorn, Andreas Blattmann, Patrick Esser, and Robin Rombach. Fast high-resolution image synthesis with latent adversarial diffusion distillation. In *Proceedings of the SIGGRAPH Asia 2024 Conference Papers (SIGGRAPH Asia)*, 2024. 3
- [43] Axel Sauer, Dominik Lorenz, Andreas Blattmann, and Robin Rombach. Adversarial diffusion distillation. In *Proceedings of the European Conference on Computer Vision (ECCV)*, 2024. 3
- [44] Jascha Sohl-Dickstein, Eric Weiss, Niru Maheswaranathan, and Surya Ganguli. Deep unsupervised learning using nonequilibrium thermodynamics. In *Proceedings of the International Conference on Learning Representations (ICLR)*, 2015. 1
- [45] Jiaming Song, Chenlin Meng, and Stefano Ermon. Denoising diffusion implicit models. In *Proceedings of the International Conference on Learning Representations (ICLR)*, 2021. 3
- [46] Jiaming Song, Qingsheng Zhang, Hongxu Yin, Morteza Mardani, Ming-Yu Liu, Jan Kautz, Yongxin Chen, and Arash Vahdat. Loss-guided diffusion models for plug-and-play controllable generation. In *Proceedings of the International Conference on Machine Learning (ICML)*, 2023. 2
- [47] Yang Song, Jascha Sohl-Dickstein, Diederik P Kingma, Abhishek Kumar, Stefano Ermon, and Ben Poole. Score-based generative modeling through stochastic differential equations. In *Proceedings of the International Conference on Learning Representations (ICLR)*, 2020. 1, 2
- [48] Yang Song, Prafulla Dhariwal, Mark Chen, and Ilya Sutskever. Consistency models. In *Proceedings of the International Conference on Machine Learning (ICML)*, 2023. 3
- [49] Lingchen Sun, Rongyuan Wu, Zhengqiang Zhang, Hongwei Yong, and Lei Zhang. Improving the stability of diffusion models for content consistent super-resolution. *arXiv preprint arXiv:2401.00877*, 2024. 2
- [50] Xiaopeng Sun, Weiqi Li, Zhenyu Zhang, Qiufang Ma, Xuhan Sheng, Ming Cheng, Haoyu Ma, Shijie Zhao, Jian Zhang, Junlin Li, et al. Opdn: Omnidirectional position-aware deformable network for omnidirectional image super-resolution. In *Proceedings of the IEEE/CVF Conference on Computer Vision and Pattern Recognition Workshops (CVPRW)*, 2023. 3
- [51] Yule Sun, Ang Lu, and Lu Yu. Weighted-to-spherically-uniform quality evaluation for omnidirectional video. *IEEE Signal Processing Letters (SPL)*, 2017. 7
- [52] Jianyi Wang, Kelvin CK Chan, and Chen Change Loy. Exploring clip for assessing the look and feel of images. In *Proceedings of the AAAI Conference on Artificial Intelligence (AAAI)*, 2023. 7
- [53] Jianyi Wang, Zongsheng Yue, Shangchen Zhou, Kelvin C.K. Chan, and Chen Change Loy. Exploiting diffusion prior for

- real-world image super-resolution. *International Journal of Computer Vision (IJCV)*, 2024. 1, 2, 7
- [54] Qian Wang, Weiqi Li, Chong Mou, Xinhua Cheng, and Jian Zhang. 360dvd: Controllable panorama video generation with 360-degree video diffusion model. In *Proceedings of the IEEE/CVF Conference on Computer Vision and Pattern Recognition (CVPR)*, 2024. 3
- [55] Xintao Wang, Liangbin Xie, Chao Dong, and Ying Shan. Real-esrgan: Training real-world blind super-resolution with pure synthetic data. In *Proceedings of the International Conference on Computer Vision Workshops (ICCVW)*. 1, 2, 6
- [56] Xintao Wang, Ke Yu, Shixiang Wu, Jinjin Gu, Yihao Liu, Chao Dong, Yu Qiao, and Chen Change Loy. Esrgan: Enhanced super-resolution generative adversarial networks. In *Proceedings of the European Conference on Computer Vision Workshops (ECCVW)*, 2018.
- [57] Yinhuai Wang, Yujie Hu, Jiwen Yu, and Jian Zhang. Gan prior based null-space learning for consistent super-resolution. In *Proceedings of the AAAI Conference on Artificial Intelligence (AAAI)*, 2022. 2
- [58] Yinhuai Wang, Jiwen Yu, and Jian Zhang. Zero-shot image restoration using denoising diffusion null-space model. In *Proceedings of the Eleventh International Conference on Learning Representations (ICLR)*, 2023. 1, 2, 3, 5
- [59] Yufei Wang, Wenhan Yang, Xinyuan Chen, Yaohui Wang, Lanqing Guo, Lap-Pui Chau, Ziwei Liu, Yu Qiao, Alex C Kot, and Bihan Wen. Sinsr: diffusion-based image super-resolution in a single step. In *Proceedings of the IEEE/CVF Conference on Computer Vision and Pattern Recognition (CVPR)*, 2024. 3
- [60] Rongyuan Wu, Lingchen Sun, Zhiyuan Ma, and Lei Zhang. One-step effective diffusion network for real-world image super-resolution. In *Proceedings of the Advances in Neural Information Processing Systems (NeurIPS)*, 2024. 3, 7
- [61] Rongyuan Wu, Tao Yang, Lingchen Sun, Zhengqiang Zhang, Shuai Li, and Lei Zhang. Seesr: Towards semantics-aware real-world image super-resolution. In *Proceedings of the IEEE/CVF Conference on Computer Vision and Pattern Recognition (CVPR)*, 2024. 1, 2, 7
- [62] Jianxiong Xiao, K. A. Ehinger, A. Oliva, and A. Torralba. Recognizing scene viewpoint using panoramic place representation. In *Proceedings of the IEEE Conference on Computer Vision and Pattern Recognition (CVPR)*, 2012. 6
- [63] Yanwu Xu, Yang Zhao, Zhisheng Xiao, and Tingbo Hou. Ufogen: You forward once large scale text-to-image generation via diffusion gans. In *Proceedings of the IEEE/CVF Conference on Computer Vision and Pattern Recognition (CVPR)*, 2024. 3
- [64] Sidi Yang, Tianhe Wu, Shuwei Shi, Shanshan Lao, Yuan Gong, Mingdeng Cao, Jiahao Wang, and Yujiu Yang. Maniqa: Multi-dimension attention network for no-reference image quality assessment. In *Proceedings of the IEEE/CVF Conference on Computer Vision and Pattern Recognition (CVPR)*, 2022. 7
- [65] Shuzhou Yang, Xuanyu Zhang, Yinhuai Wang, Jiwen Yu, Yuhan Wang, and Jian Zhang. Diffle: Diffusion-based domain calibration for weak supervised low-light image enhancement. *International Journal of Computer Vision*, pages 1–20, 2024. 2
- [66] Tao Yang, Rongyuan Wu, Peiran Ren, Xuansong Xie, and Lei Zhang. Pixel-aware stable diffusion for realistic image super-resolution and personalized stylization. In *Proceedings of the European Conference on Computer Vision (ECCV)*, 2024. 1, 2
- [67] Zhixiong Yang, Jingyuan Xia, Shengxi Li, Xinghua Huang, Shuanghui Zhang, Zhen Liu, Yaowen Fu, and Yongxiang Liu. A dynamic kernel prior model for unsupervised blind image super-resolution. In *Proceedings of the IEEE/CVF Conference on Computer Vision and Pattern Recognition (CVPR)*, 2024. 4
- [68] Tianwei Yin, Michaël Gharbi, Taesung Park, Richard Zhang, Eli Shechtman, Fredo Durand, and William T Freeman. Improved distribution matching distillation for fast image synthesis. In *Proceedings of the Advances in Neural Information Processing Systems (NeurIPS)*, 2024. 3
- [69] Fanghua Yu, Xintao Wang, Mingdeng Cao, Gen Li, Ying Shan, and Chao Dong. Osrt: Omnidirectional image super-resolution with distortion-aware transformer. In *Proceedings of the IEEE/CVF Conference on Computer Vision and Pattern Recognition (CVPR)*, 2023. 1, 3, 4, 6, 7
- [70] Fanghua Yu, Jinjin Gu, Zheyuan Li, Jinfan Hu, Xiangtao Kong, Xintao Wang, Jingwen He, Yu Qiao, and Chao Dong. Scaling up to excellence: Practicing model scaling for photo-realistic image restoration in the wild. In *Proceedings of the IEEE/CVF Conference on Computer Vision and Pattern Recognition (CVPR)*, 2024. 2, 3
- [71] Zongsheng Yue, Jianyi Wang, and Chen Change Loy. Resshift: Efficient diffusion model for image super-resolution by residual shifting. In *Proceedings of the Advances in Neural Information Processing Systems (NeurIPS)*, 2023. 3
- [72] Aiping Zhang, Zongsheng Yue, Renjing Pei, Wenqi Ren, and Xiaochun Cao. Degradation-guided one-step image super-resolution with diffusion priors. *arXiv preprint arXiv:2409.17058*, 2024. 1, 3, 4, 6, 7
- [73] Jian Zhang and Bernard Ghanem. Ista-net: Interpretable optimization-inspired deep network for image compressive sensing. In *Proceedings of the IEEE Conference on Computer Vision and Pattern Recognition (CVPR)*, 2018. 3
- [74] Richard Zhang, Phillip Isola, Alexei A Efros, Eli Shechtman, and Oliver Wang. The unreasonable effectiveness of deep features as a perceptual metric. In *Proceedings of the IEEE Conference on Computer Vision and Pattern Recognition (CVPR)*, 2018. 7
- [75] Xiangyu Zhang, Xinyu Zhou, Mengxiao Lin, and Jian Sun. Shufflenet: An extremely efficient convolutional neural network for mobile devices. In *Proceedings of the IEEE Conference on Computer Vision and Pattern Recognition (CVPR)*, 2018. 5
- [76] Yufeng Zhou, Mei Yu, Hualin Ma, Hua Shao, and Gangyi Jiang. Weighted-to-spherically-uniform ssim objective quality evaluation for panoramic video. In *Proceedings of the IEEE International Conference on Signal Processing (ICSP)*, 2018. 7

RealOSR: Latent Unfolding Boosting Diffusion-based Real-world Omnidirectional Image Super-Resolution

Supplementary Material

Method	Inference Time (s)	#Params (M)
S3Diff	10.42	1326.76
SeeSR	42.32	2249.91
OmniSSR	511.70	1554.64
StableSR	162.96	1554.64
RealOSR-s	6.85	1352.20
RealOSR-p	2.36	1352.20

Table 5. Efficiency comparison with diffusion-based methods regarding parameter count ($1M = 1 \times 10^6$) and inference time (second) per ERP image. “RealOSR-s” represents **serial** SR of all TP images. And “RealOSR-p” represents **parallel** SR of them. The best and second-best results are shown in **red** and **blue**.

We conducted extra experiments to demonstrate the practical competitiveness of RealOSR in the real-world omnidirectional image (ODI) super-resolution (SR) scenarios.

A. Efficiency of the Compared Approaches

RealOSR achieves significantly faster inference than other diffusion-based methods due to its efficient single-step denoising design (in Tab. 5). Although TP images have more pixels than a corresponding ERP image, each TP image has a lower resolution, facilitating faster processing in RealOSR. In contrast, existing methods process ODIs using a shifting-window strategy, introducing significant computational redundancy from overlapping windows on the ERP image.

Furthermore, parallel SR of multiple TP images further enhances the running speed of RealOSR, reducing inference time to **2.36 seconds** on a NVIDIA 4090 GPU.

Apart from degradation-aware LoRA, RealOSR introduces only **25.44M** additional parameters for the Deep Unfolding Injector Guidance (DUIG) modules. Some methods (e.g., SeeSR) employ a ControlNet-like approach to inject LR image information, resulting in a model parameter count of the same order as the SD UNet. The DUIG is more lightweight while maintaining efficient inference.

B. Robustness of the Compared Approaches

We assess the robustness of various methods under more severe degradation conditions. This involves increasing JPEG compression and random noise levels in the input images. As shown in Tab. 6, RealOSR exhibits **superior** and **consistent** SR performance (FID: 43.39 \rightarrow 49.31) under more severe degradation, significantly outperforming other approaches such as S3Diff (FID: 85.01 \rightarrow 124.14). This highlights the robustness of our approach in handling varying levels of degradation encountered in real-world scenarios.

C. Limitations of Non-Reference Metrics for ODISR

Tab. 2 in the main paper shows that SeeSR performs comparably on NIQE, MUSIQ, MANIQA, and CLIPQA. However, visualizations provided in Fig. 8 and Fig. 9 indicate that while SeeSR generates well-defined images, it fails to preserve fidelity to the original low-resolution input. Although non-reference metrics such as NIQE, MUSIQ, MANIQA, and CLIPQA provide quantitative insights into image quality, they fail to fully capture the fidelity and perceptual consistency required for omnidirectional image super-resolution. Therefore, future work could explore the development of evaluation metrics specifically tailored for omnidirectional image super-resolution.

D. Towards Real-world 8K-Level SR

The HR ERP images in existing datasets only have a resolution of 1024×2048 , whereas real-world ODI applications require $4K \times 8K$ resolution for practical use. It remains uncertain whether these methods are applicable to real-world omnidirectional image super-resolution (Real-ODISR). Therefore, in this section, we evaluate existing models by regarding HR ERP images from the dataset as LR input images to generate $4K \times 8K$ SR results.

We employ non-reference metrics (NIQE, MUSIQ, MANIQA, CLIPQA) for evaluation, as no ground truth is available for the SR results. As discussed in the main paper, the non-reference metrics are designed for planar images and may not fully reflect the SR performance on ODIs. To evaluate SR performance more fairly, we compute non-reference metrics on TP images derived from super-resolved ERP images, referred to as TP-NIQE, TP-MUSIQ, TP-MANIQA, and TP-CLIPQA. As shown in Tab. 7, our RealOSR achieves superior performance across all metrics, **demonstrating its effectiveness (including the proposed model architecture and training data construction pipeline) for Real-ODISR**. The 8K SR visual results of RealOSR on the ODI-SR dataset can be referred to Figs. 10 and 11.

Datasets	Methods	WS-PSNR \uparrow	WS-SSIM \uparrow	LPIPS \downarrow	DISTS \downarrow	FID \downarrow	NIQE \downarrow	MUSIQ \uparrow	MANIQA \uparrow	CLIPQA \uparrow
SUN 360	S3Diff	20.42	0.4066	0.5194	0.1903	124.14	3.3758	67.44	0.4907	0.5055
	SeeSR	19.75	0.5799	0.4523	0.2193	129.43	5.1846	70.58	0.5560	0.7011
	OmniSSR	20.59	0.3975	0.7945	0.3312	188.04	7.9905	27.66	0.2227	0.2339
	StableSR	21.36	0.4821	0.5526	0.2138	139.79	3.1281	57.09	0.2946	0.3844
	OSDiff	21.36	0.5300	0.4397	0.1775	112.36	3.4903	68.94	0.4898	0.5461
	RealOSR (Ours)	22.25	0.5967	0.3155	0.1096	49.31	3.4860	70.02	0.4245	0.6004

Table 6. Quantitative comparison of diffusion-based methods **under more severe degradation conditions**. The best and second-best results are highlighted in **red** and **blue**. This demonstrates the robustness of RealOSR in addressing varying degrees of degradation in real-world scenarios.

Datasets	Methods	NIQE \downarrow	MUSIQ \uparrow	MANIQA \uparrow	CLIPQA \uparrow	TP-NIQE \downarrow	TP-MUSIQ \uparrow	TP-MANIQA \uparrow	TP-CLIPQA \uparrow
ODI-SR	S3Diff	4.1327	41.45	0.4100	0.6509	5.0126	51.25	0.3567	0.6146
	StableSR	3.7976	35.40	0.3572	0.4883	5.5994	45.11	0.3323	0.4988
	RealOSR (Ours)	3.3745	42.63	0.4105	0.6433	5.4382	54.08	0.3682	0.6544

Table 7. Quantitative comparison of diffusion-based methods on **8K SR** by taking ground truth in ODI-SR test-set as LR input. The best and second-best results are highlighted in **red** and **blue**. Our RealOSR has a strong generalization ability to 8K-level Real-ODISR.

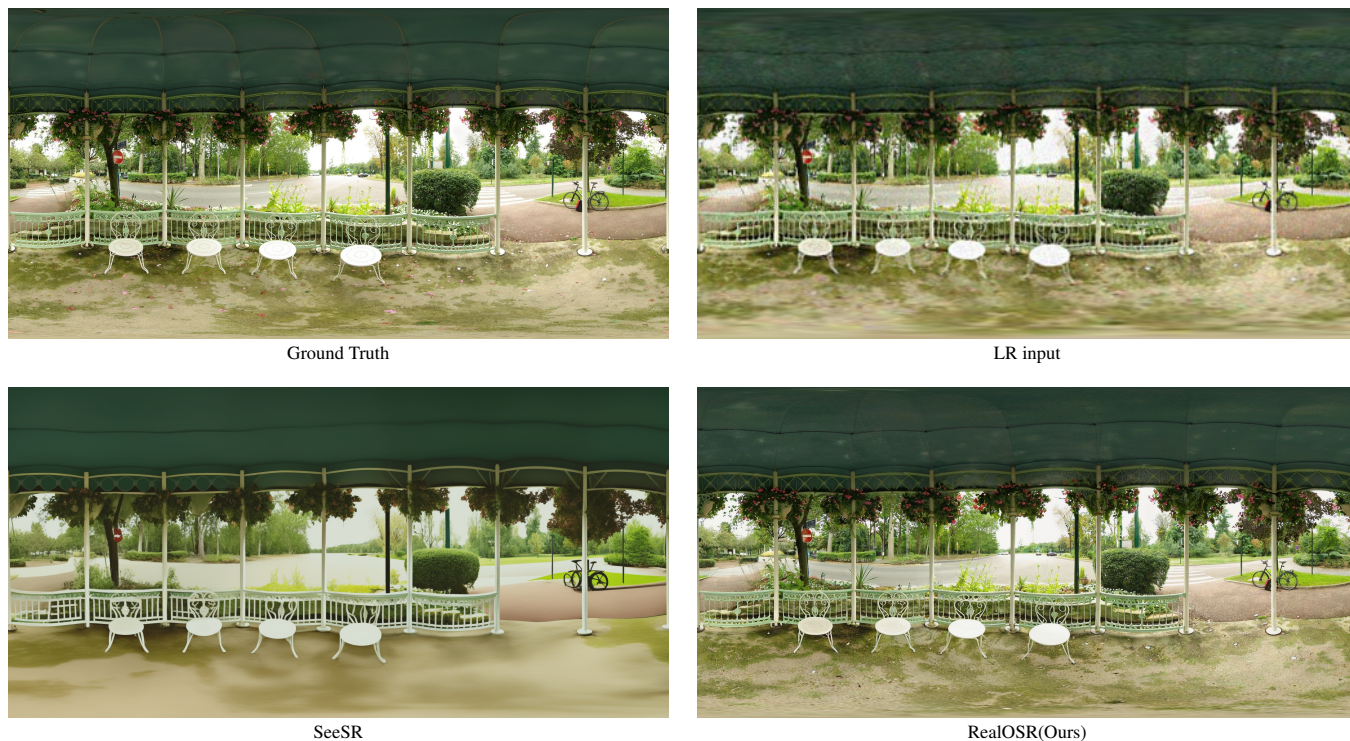


Figure 8. Visualized comparison of SeeSR and our RealOSR on **ODI-SR test-set 0000**.

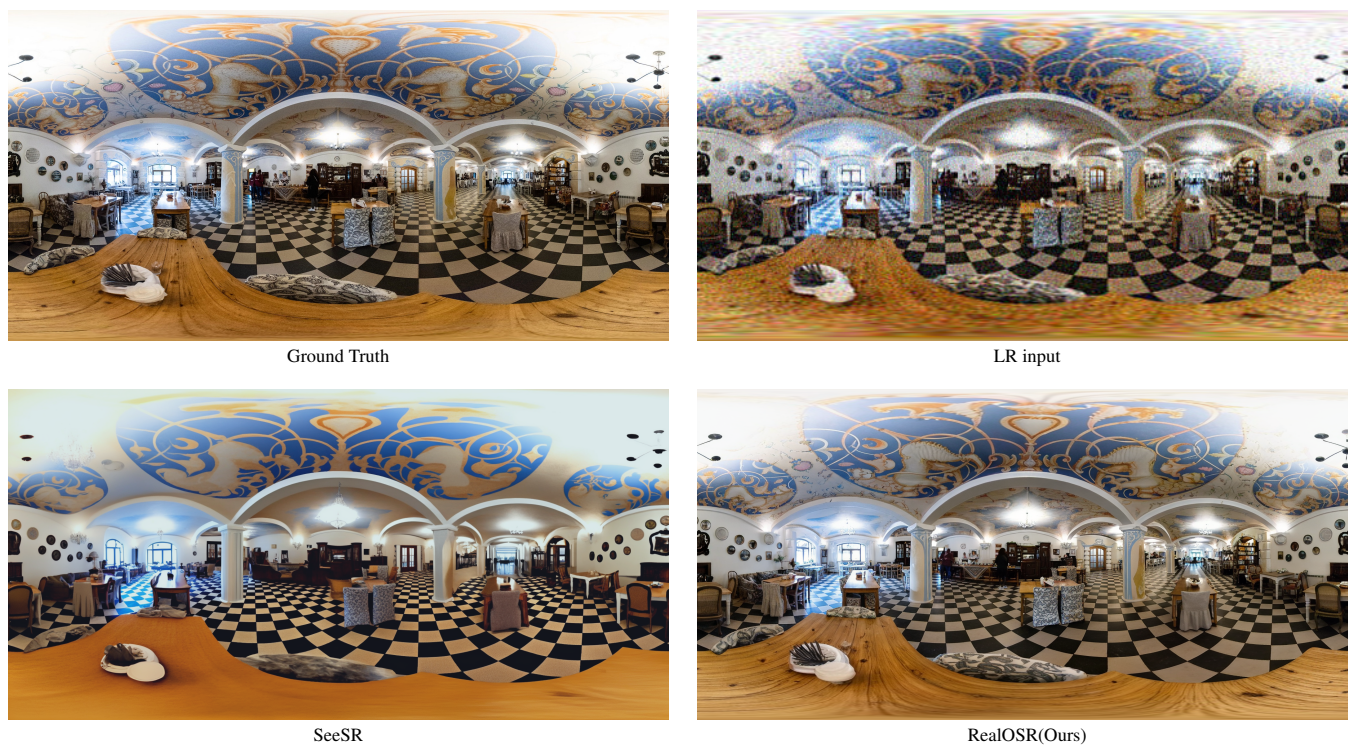


Figure 9. Visualized comparison of SeeSR and our RealOSR on **ODI-SR test-set 0067**.



Figure 10. SR results of RealOSR on **ODI-SR 0028** at **4096 × 8192** resolution.



Figure 11. SR results of RealOSR on **ODI-SR 0097** at **4096 × 8192** resolution.